Dust settling against hydrodynamic turbulence in protoplanetary discs

Min-Kai Lin ⭐

Institute of Astronomy and Astrophysics, Academia Sinica, Taipei 10617, Taiwan

ABSTRACT

Enhancing the local dust-to-gas ratio in protoplanetary discs is a necessary first step to planetesimal formation. In laminar discs, dust settling is an efficient mechanism to raise the dust-to-gas ratio at the disc mid-plane. However, turbulence, if present, can stir and lift dust particles, which ultimately hinders planetesimal formation. In this work, we study dust settling in protoplanetary discs with hydrodynamic turbulence sustained by the vertical shear instability. We perform axisymmetric numerical simulations to investigate the effect of turbulence, particle size, and solid abundance or metallicity on dust settling. We highlight the positive role of drag forces exerted on to the gas by the dust for settling to overcome the vertical shear instability. In typical disc models we find particles with a Stokes number $\sim 10^{-3}$ can sediment to $\lesssim 10$ per cent of the gas scaleheight, provided that $\Sigma_d/\Sigma_g \gtrsim 0.02$–$0.05$, where $\Sigma_{d,g}$ are the surface densities in dust and gas, respectively. This coincides with the metallicity condition for small particles to undergo clumping via the streaming instability. Supersolar metallicities, at least locally, are thus required for a self-consistent picture of planetesimal formation. Our results also imply that dust rings observed in protoplanetary discs should have smaller scaleheights than dust gaps, provided that the metallicity contrast between rings and gaps exceed the corresponding contrast in gas density.

Key words: accretion, accretion discs – hydrodynamics – methods: numerical – protoplanetary discs.

1 INTRODUCTION

In the standard 'core accretion' scenario, planets are formed by the aggregation of km-sized or larger planetesimals via their mutual gravitational attraction (Safronov 1969; Lissauer 1993; Helled et al. 2014; Raymond et al. 2014). The precursor to planet formation is therefore planetesimal formation (Chiang & Youdin 2010). However, solids in protoplanetary discs (PPDs) begin as micron-sized dust. These small grains can grow to mm–cm sizes by sticking, but collisional growth beyond this size is limited by bouncing or fragmentation (Blum 2018). Other effects, such as turbulence or radial drift, can also hinder particle growth (Johansen et al. 2014).

One way to circumvent these growth barriers is to invoke the collective gravitational collapse of a population of dust grains (Goldreich & Ward 1973). A dynamical gravitational instability (GI) in dust requires a high dust-to-gas ratios, $\rho_d/\rho_g \gg 1$, where ρ_d and ρ_g are the dust and gas mass densities, respectively (Chiang & Youdin 2010; Shi & Chiang 2013). However, in a newly formed PPD, where dust and gas are well-mixed, we expect $\rho_d/\rho_g \sim 10^{-2}$ everywhere, as typical of the dust-to-gas mass ratio in the interstellar medium. Thus, to trigger GI for planetesimal formation,

dust grains must first be concentrated to sufficiently high volume densities relative to the gas.

A promising mechanism for concentrating dust is the streaming instability (SI; Youdin & Goodman 2005; Youdin & Johansen 2007). The SI naturally arises from the mutual dust-gas drag in rotating discs (Jacquet, Balbus & Latter 2011), and is driven by the relative drift between dust and gas caused by radial pressure gradients. More recent physical interpretations of the SI have been given by Lin and Youdin (2017, hereafter LY17), and Squire and Hopkins (2018).

In principle, the SI can occur at any dust-to-gas ratios, but for small particles the SI grows slowly under dust-poor conditions ($\rho_d \lesssim \rho_g$). Furthermore, in this limit the SI does not lead to dust clumping (Johansen & Youdin 2007). Indeed, numerical simulations show strong clumping, and hence planetesimal formation, only when $\rho_d \gtrsim \rho_g$ (e.g. Johansen, Youdin & Mac Low 2009b; Bai & Stone 2010a,b; Simon et al. 2016; Yang, Johansen & Carrera 2017). How to realize this optimal condition for the SI, at least locally in a PPD, is therefore a crucial issue for planet formation.

Several other dust-concentrating mechanisms may act to seed the SI (Chiang & Youdin 2010; Johansen et al. 2014). These include dust-trapping by pressure bumps, zonal flows, and vortices (Barge & Sommeria 1995; Johansen, Youdin & Klahr 2009a; Dittrich, Klahr & Johansen 2013; Lyra & Lin 2013; Raettig, Klahr & Lyra 2015; Pinilla & Youdin 2017), gas removal by

photoevaporation or disc winds (Alexander et al. 2014; Bai 2016), other dust-gas drag instabilities (Takahashi & Inutsuka 2014; Gonzalez, Laibe & Maddison 2017), radial pile-up of dust (Kanagawa et al. 2017), and dust settling (Nakagawa, Sekiya & Hayashi 1986; Dubrulle, Morfill & Sterzik 1995; Takeuchi & Lin 2002). Some of these processes may directly induce GI in dust without going through SI.

In this work we focus on dust settling. This is perhaps the simplest way to increase ρ_d/ρ_g: dust particles sediment towards the disc mid-plane due to the vertical component of stellar gravity and drag forces from the gas. However, dust settling requires the disc to be sufficiently laminar (Dubrulle et al. 1995; Youdin & Lithwick 2007). Otherwise, turbulence can stir up the particles. Turbulence may arise from the settling process itself, for example via Kelvin–Helmholtz instabilities associated with the differential rotation between the dust and gas layers (KHI; Johansen, Henning & Klahr 2006; Chiang 2008; Barranco 2009; Lee et al. 2010), or weak SI (Johansen & Youdin 2007; Bai & Stone 2010a). In these cases, ρ_d/ρ_g may be self-limited and never reach unity.

Furthermore, there are external sources of turbulence in PPDs. Magnetic instabilities (Balbus & Hawley 1991) and gaseous GI (Gammie 2001) can have significant impact on dust dynamics (e.g. Rice et al. 2004; Fromang & Papaloizou 2006; Balsara et al. 2009; Gibbons, Rice & Mamatsashvili 2012; Zhu, Stone & Bai 2015; Shi, Zhu, Stone & Chiang 2016; Riols & Lesur 2018; Yang, Mac Low & Johansen 2018).

In addition, there is a plethora of newly (re)discovered, purely hydrodynamic instabilities that drive turbulence (Fromang & Lesur 2017; Klahr, Pfeil & Schreiber 2018; Lyra & Umurhan 2018). These include: the zombie vortex instability (Marcus et al. 2015; Lesur & Latter 2016; Umurhan, Shariff & Cuzzi 2016), the convective overstability (Klahr & Hubbard 2014; Lyra 2014; Latter 2016), and the vertical shear instability (VSI; Nelson, Gressel & Umurhan 2013; Barker & Latter 2015; Lin & Youdin 2015, hereafter LY15). These instabilities are relevant to magnetically inactive or non-self-gravitating regions of the disc. Among them, the VSI is particularly relevant to dust settling.

The VSI taps into the free energy associated with a vertical gradient in the gaseous disc's angular velocity Ω (LY15; Barker & Latter 2015). Such a vertical shear, $\partial_z \Omega \neq 0$, arises whenever the gas is baroclinic. This is the case in the outer parts of PPDs where a non-uniform radial temperature profile is set by stellar irradiation (Stoll & Kley 2014). The VSI is characterized by large-scale vertical motions (Nelson et al. 2013) and the associated stress is much stronger than that in the radial direction (Stoll, Kley & Picogna 2017). It is then natural to question whether or not dust particle can still settle to the point of triggering rapid SI.

Recent numerical simulations have begun to study the influence of the VSI on particle dynamics in PPDs (Stoll & Kley 2016; Flock et al. 2017). These studies find that small particles with sizes $\lesssim$ mm can be efficiently lifted by VSI turbulence. However, these studies model dust as passive particles, i.e. the back-reaction of dust-drag on to the gas is neglected. However, this feedback would induce an effective buoyancy force, as the dust adds weight to the mixture but not pressure (LY17). On the other hand, buoyancy is known to be effective in stabilizing the VSI (LY15). It is thus necessary to include particle back-reaction on to the gas to study dust settling against VSI turbulence.

In this work, we study dust settling against the VSI by applying LY17's thermodynamic model of dusty PPDs, which implicitly includes particle back-reaction. This allows us to investigate the effect of the overall solid abundance on dust settling in VSI-active

discs. LY17's framework was previously applied to study dusty disc–planet interaction (Chen & Lin 2018; hereafter CL18). Here we adapt CL18's numerical models.

This paper is organized as follows. In Section 2 we briefly review the governing equations of LY17 and CL18, which forms the basis of this work. We then describe our initial disc models in Section 3. Our numerical set-up is described in Section 4, along with several diagnostics. We present simulation results in Section 5. We find that dust settling can overcome the VSI if the local metallicity, Σ_d/Σ_g, where $\Sigma_{d,g}$ are dust and gas surface densities, respectively, is a few times above the solar value. We interpret and discuss our results in Section 6, including its implication for planetesimal formation and observations of PPDs. We conclude and summarize in Section 7.

2 BASIC EQUATIONS

We consider an accretion disc comprised of gas and dust orbiting a central star of mass M_*. We neglect disc self-gravity, magnetic fields, and viscosity. Cylindrical (R, ϕ, z) and spherical (r, θ, ϕ) coordinates are centred on the star. In the discussions below, we use subscript '0' to denote evaluation at (R, z) = (R_0, 0), where R_0 is a reference radius. The Keplerian frequency is $\Omega_K(R) \equiv \sqrt{GM_*/R^3}$, where G is the gravitational constant. We adopt a rotating frame with angular frequency $\Omega_{K0}\hat{z}$.

The gas phase has density, pressure, and velocity fields (ρ_g, P, $\boldsymbol{v}_g$). We model a single species of dust particles as a second, pressureless fluid with mass density and velocity (ρ_d, $\boldsymbol{v}_d$). The fluid approximation for dust is valid for sufficiently small particles (Jacquet et al. 2011).

We also define the total mass density,

$$\rho \equiv \rho_g + \rho_d, \tag{1}$$

the centre-of-mass velocity ,

$$\boldsymbol{v} \equiv \frac{\rho_d \boldsymbol{v}_d + \rho_g \boldsymbol{v}_g}{\rho}, \tag{2}$$

and an effective energy ,

$$E \equiv \frac{P}{\gamma - 1} + \frac{1}{2}\rho|\boldsymbol{v}|^2 + \rho\Phi, \tag{3}$$

where γ is a constant defined below and Φ is a time-independent gravitational potential ($\partial_t \Phi = 0$). Our numerical simulations evolve the hydrodynamic set (ρ, $\boldsymbol{v}$, E); see Section 2.3.

2.1 Polytropic gas

We consider a locally polytropic gas with

$$P = c_s^2(R)\rho_{g0}\left(\frac{\rho_g}{\rho_{g0}}\right)^\gamma \equiv K(R)\rho_g^\gamma, \tag{4}$$

where $c_s(R)$ is a prescribed sound-speed profile and γ is the constant polytropic index. We take $\gamma = 1.001$ so the gas is nearly isothermal in its thermodynamic property. We set

$$c_s^2(R) = c_{s0}^2\left(\frac{R}{R_0}\right)^{-q}, \tag{5}$$

where q is the constant temperature profile index. Such a temperature profile is said to be locally or vertically isothermal. We also define the pressure scaleheight H_g

$$H_g \equiv \frac{c_s}{\Omega_K}, \tag{6}$$

and the gas disc aspect ratio is $h_g \equiv H_g/R$.

2.2 Tightly coupled dust

The dust fluid interacts with the gas via a drag force characterized by the particle stopping time τ_s. We consider particles in the Epstein regime with $\tau_s = \rho_\bullet s / \rho_g c_s$ (Weidenschilling 1977), where $\rho_\bullet$, s is the internal density and radius of a grain, respectively.

However, in the one-fluid framework adopted below, it is convenient to define the *relative* stopping time $t_s = \tau_s \rho_g / \rho$ (Laibe & Price 2014a). This is the characteristic decay time-scale for the relative drift between dust and gas, $|v_d - v_g|$, due to the mutual drag forces. The Stokes number can be defined as $t_s \Omega_K$.

We parametrize t_s via a dimensionless stopping time T_{stop} such that

$$t_s = \frac{\rho_\bullet s}{\rho c_s} \equiv \frac{\rho_0 c_{s0}}{\rho c_s} \frac{T_{stop}}{\Omega_{K0}}. \tag{7}$$

Thus $T_{stop} = \Omega_{K0} \rho_\bullet s / \rho_0 c_{s0}$ is also the Stokes number for a particle of a given size and internal density at the reference point. For convenience we will also refer to T_{stop} as the particle size.

In addition, we consider small particles with

$$t_s \Omega_K \ll 1. \tag{8}$$

In this limit dust particles are tightly, but not necessarily perfectly, coupled to the gas; and one can relate dust and gas velocities by the *terminal velocity approximation*:

$$v_d = v_g + t_s \frac{\nabla P}{\rho_g} \tag{9}$$

(Youdin & Goodman 2005; Jacquet et al. 2011; Price & Laibe 2015, LY17). Note that a differential Coriolis force has been neglected in equation (9) as it is of order t_s^2 (see e.g. Laibe & Price 2014b). Equation (9) reflects the fact that particles tend to drift towards pressure maxima (Whipple 1972; Weidenschilling 1977).

2.3 Evolutionary equations

With the above definitions and approximations, LY17 and CL18, building upon Laibe and Price (2014a), showed that the dusty gas disc can be described by the following evolutionary equations:

$$\frac{\partial \rho}{\partial t} + \nabla \cdot (\rho v) = 0, \tag{10}$$

$$\frac{\partial v}{\partial t} + v \cdot \nabla v = -\frac{1}{\rho} \nabla P - \nabla \Phi - 2\Omega_{K0} \hat{z} \times v, \tag{11}$$

$$\begin{aligned} \frac{\partial E}{\partial t} + \nabla \cdot [(E + P)v] &= \frac{P}{\gamma - 1} v \cdot \nabla \ln c_s^2 \\ &+ \frac{\gamma P}{\rho_g(\gamma - 1)} \nabla \cdot (f_d t_s \nabla P), \end{aligned} \tag{12}$$

where the dust fraction $f_d \equiv \rho_d / \rho$ can be obtained from the equation of state (equation 4)

$$f_d = 1 - \frac{1}{\rho} \left(\frac{P}{K} \right)^{1/\gamma}, \tag{13}$$

and $\rho_g = (1 - f_d)\rho$. We define the dust-to-gas ratio $\epsilon \equiv \rho_d / \rho_g = f_d / (1 - f_d)$. A similar one-fluid model was also adopted by Fromang and Papaloizou (2006) to simulate dusty, magnetized discs.

In the rotating frame the total gravitational potential is

$$\Phi(R, \phi, z) = \Phi_*(R, z) - \frac{1}{2} R^2 \Omega_{K0}^2. \tag{14}$$

Here,

$$\Phi_*(R, z) = -R^2 \Omega_K^2 \left(1 - \frac{z^2}{2R^2} \right). \tag{15}$$

is the stellar potential in the thin-disc approximation ($|z| \ll R$). We adopt this approximate form in order specify initial conditions analytically.

Equations (10)–(12) provide a hydrodynamic description of the dusty gas. The dust density is recovered from the equation of state (4), and the dust velocity from the terminal velocity approximation ($v_d = v + t_s \nabla P / \rho$). Equations (10)–(11) physically corresponds to mass and momentum conservation for the mixture.

However, equation (12) is not a physical energy equation. It simply stems from dust mass conservation, the equation of state, and the terminal velocity approximation (LY17, CL18). The term $\propto \nabla c_s^2$ on the right-hand side models the rapid cooling that enforces a locally (vertically) isothermal temperature profile, and is the term responsible for the VSI. The second term on the right-hand side models dust-gas decoupling.

2.4 Dusty entropy and buoyancy

Describing the dusty gas in terms of the hydrodynamic variables (ρ, v, P) allows us to define the (dimensionless) effective entropy of the system as

$$S \equiv \ln \frac{P^{1/\gamma}}{\rho} = \ln c_s^{2/\gamma} - \ln(1 + \epsilon) + \text{const.} \tag{16}$$

(LY17). A non-uniform entropy profile produces buoyancy forces. For this work the relevant quantity is the squared vertical buoyancy frequency

$$N_z^2 \equiv -\frac{1}{\rho} \frac{\partial P}{\partial z} \frac{\partial S}{\partial z} = \frac{1}{1 + \epsilon} \frac{1}{\rho} \frac{\partial P}{\partial z} \frac{\partial \epsilon}{\partial z}, \tag{17}$$

where the second equality applies to the vertically isothermal temperature profiles we consider.

The notion of a dust-induced buoyancy is most applicable to dust perfectly coupled to the gas. In this limit, dust particles add to the mixture's inertia but not the pressure. Dust therefore 'weighs down' the fluid. Hence there is an associated buoyancy force. Settled dust provides a stabilizing force against vertical motions of the VSI since $N_z^2 > 0$ in that case (see also Section 3.2).

However, settling in the first place requires some decoupling between dust and gas. This diminishes the effective buoyancy as dust can slip past the gas. The definition above should thus be interpreted as the maximum buoyancy induced by dust.

3 DISC MODELS

We initialize our discs by first specifying the dust-to-gas ratio distribution

$$\epsilon(R, z) = \epsilon_{mid}(R) \times \exp \left(-\frac{z^2}{2H_\epsilon^2} \right). \tag{18}$$

Here and below subscript 'mid' indicates the mid-plane value. The profile $\epsilon_{mid}(R)$ is chosen to minimize radial disc evolution, as described in Appendix B of CL18. The characteristic thickness in the dust-to-gas ratio, H_ϵ, is defined via

$$\frac{1}{H_\epsilon^2} \equiv \frac{1}{H_d^2} - \frac{1}{H_g^2}. \tag{19}$$

Here the dust layer thickness H_d is set to $0.99H_g$ so that initially the dust is vertically well-mixed with the gas ($H_\epsilon \gg 1$). For $t > 0$ we fit

the vertical dust density distribution to a Gaussian profile to obtain H_d (see Section 4.2).

We scale the dust-to-gas ratio by specifying the metallicity Z at the reference radius

$$Z \equiv \left. \frac{\Sigma_d}{\Sigma_g} \right|_0 = \epsilon_{mid} \left. \frac{H_d}{H_g} \right|_0, \quad (20)$$

(Johansen et al. 2014). Recall $\Sigma_{d,g}$ are the surface densities in dust and gas, respectively.

We obtain the disc structure by assuming dynamical equilibrium and axisymmetry:

$$R\Omega^2 = R\Omega_K^2 \left(1 - \frac{3}{2} \frac{z^2}{R^2} \right) + \frac{1}{\rho} \frac{\partial P}{\partial R}, \quad (21)$$

$$0 = z\Omega_K^2 + \frac{1}{\rho} \frac{\partial P}{\partial z}. \quad (22)$$

Here $\Omega \equiv v_\phi / R + \Omega_{K0}$ is the angular velocity in the inertial frame. For simplicity we set $\gamma = 1$ to integrate equation (22), making use of equation (18), to obtain

$$\rho_g = \rho_{g,mid} \exp\left\{ -\frac{z^2}{2H_g^2} - \epsilon_{mid} \frac{H_\epsilon^2}{H_g^2} \left[1 - \exp\left(-\frac{z^2}{2H_\epsilon^2} \right) \right] \right\}. \quad (23)$$

We set the mid-plane gas density to

$$\rho_{g,mid}(R) = \frac{\Sigma_g(R)}{\sqrt{2\pi} H_g(R)}, \quad (24)$$

with gas surface density

$$\Sigma_g(R) = \Sigma_{g0} \left(\frac{R}{R_0} \right)^{-p}, \quad (25)$$

and we fix $p = 3/2$. The total density is $\rho = \rho_g(1 + \epsilon)$. Finally, the disc orbital frequency is obtained from equation (21),

$$\Omega(R, z) = \Omega_K \left[1 - \frac{3}{2} \frac{z^2}{R^2} + \frac{P}{\rho (R\Omega_K)^2} \left(\gamma \frac{\partial \ln \rho_g}{\partial \ln R} - q \right) \right]^{1/2}. \quad (26)$$

3.1 Vertical shear

The disc rotation possesses vertical shear. This can be seen directly from equations (21)–(22):

$$R\frac{\partial \Omega^2}{\partial z} = \frac{c_s^2(R)}{(1 + \epsilon)^2} \left\{ \frac{\partial \epsilon}{\partial R} \frac{\partial \ln \rho_g}{\partial z} - \frac{\partial \epsilon}{\partial z} \frac{\partial \ln P}{\partial R} \right. $$
$$\left. + \frac{q}{R} (1 + \epsilon) \frac{\partial \ln \rho_g}{\partial z} \right\}. \quad (27)$$

Vertical shear can thus arise from a non-uniform dust-to-gas ratio distributions (the first two terms), and from the imposed radial temperature gradient (the last term). However, LY17 showed that gradients in ϵ generally do not lead to axisymmetric instabilities in PPDs, unless sharp radial edges are present. For axisymmetric models, as will be adopted below, dust settling in radially smooth discs only contributes to stabilization via vertical buoyancy forces (cf. the non-axisymmetric KHI, see Chiang 2008). The VSI in our simulations are associated with the imposed radial temperature gradient.

3.2 Buoyant stabilization

We expect the VSI to be affected by buoyancy forces when the buoyancy frequency becomes comparable to the vertical shear rate

such that

$$N_z^2 \gtrsim \left| R \frac{\partial \Omega^2}{\partial z} \right|_{temp} \equiv \frac{|q| c_s^2}{(1 + \epsilon) R} \left| \frac{\partial \ln \rho_g}{\partial z} \right|, \quad (28)$$

(LY15), where the right-hand side is the last term in equation (27). This is the only destabilizing effect in axisymmetric discs in the limit of vanishing particle size (LY17). Evaluating this inequality using equation (17) gives

$$\frac{1}{(1 + \epsilon)} \left| \frac{\partial \epsilon}{\partial z} \right| \gtrsim \frac{|q|}{R}. \quad (29)$$

For the ϵ profiles we adopt (equation 18), we have $|\partial_z \epsilon| \sim \epsilon_{mid} / H_\epsilon$. Then, considering the fiducial radius without loss of generality, we expect dust-induced buoyancy becomes important for mid-plane dust-to-gas ratios

$$\epsilon_0 \gtrsim h_g |q| \frac{H_d}{H_g}, \quad (30)$$

for somewhat settled dust ($H_d \lesssim H_g$), where the definition equation (19) was used. Thus we can expect dust-induced buoyant stabilization of the VSI even when $\epsilon_0 \sim h_g |q| \ll 1$. LY17 give a similar estimate and confirm it with linear stability calculations (see their sections 6.1–6.2).

The VSI is sensitive to dust-loading because the temperature-induced, destabilizing vertical shear is weak, so even a small amount of dust-induced buoyancy can stabilize it (Nelson et al. 2013; LY15; LY17). We give a numerical example of this effect in Appendix A.

4 NUMERICAL SIMULATIONS

We carry out global, axisymmetric numerical simulations using the PLUTO hydrodynamics code (Mignone et al. 2007, 2012), modified to evolve the dust-free model equations (10)–(12), as described in CL18. We configure PLUTO with piecewise linear reconstruction, the HLLC Riemann solver, and second-order Runge–Kutta time integration. We found this default set-up to be robust,[1] but its diffusive nature likely suppresses the streaming instability.

We adopt spherical coordinates with $r \in [0.6, 1.4]R_0$ and a polar angle range such that $\tan(\pi/2 - \theta) \in [-2, 2]h_{g0}$, i.e. two gas scaleheights above and below the disc mid-plane at the reference radius. We fix $h_{g0} = 0.05$. The standard resolution is $N_r \times N_\theta = 1920 \times 480$; with logarithmic and uniform spacing in r and θ, respectively. This corresponds to a resolution of approximately 100 cells per H_g at $R = R_0$. We impose reflective boundary conditions in θ, and set radial boundary ghost zones to their initial values.

4.1 Physical parameters

Our fiducial parameter values are $q = 1$, $T_{stop} = 10^{-3}$, and $Z = 10^{-2}$. As shown below, VSI turbulence prevents dust settling for this set-up. We are interested in how these parameters can be varied to enable settling:

(i) We vary the imposed radial temperature gradient $q \in [0, 1]$. Smaller $|q|$ decreases the strength of the VSI turbulence and is expected to help settling.

---

[1]Test simulations with piecewise parabolic interpolation, a Roe solver, and third-order Runge–Kutta time integration produced numerical artefacts near the vertical boundaries.

(ii) We vary the stopping time $T_{\text{stop}} \in [10^{-3}, 10^{-2}]$. Larger T_{stop}, corresponding to larger particles, is expected to settle faster and avoid stirring by the VSI, at least initially.

(iii) We vary the overall metallicity $Z \in [10^{-2}, 10^{-1}]$. Increasing Z is expected to stabilize the VSI and favour settling.

For comparison, the oft-used minimum mass solar nebula (MMSN) has a shallower temperature profile with $q = 0.43$ and is slightly more dusty at $Z = 0.015$ (Chiang & Youdin 2010) than our fiducial set-up. Epstein drag stopping times in MMSN-like disc models vary as

$$T_{\text{stop}} \simeq \frac{10^{-3}}{F} \left(\frac{s}{100\,\mu\text{m}} \right) \left(\frac{\rho_\bullet}{\text{g cm}^{-3}} \right) \left(\frac{R_0}{20\,\text{au}} \right)^{3/2}, \quad (31)$$

where F is the mass scale relative to the MMSN. At fixed T_{stop}, smaller particles reside at larger distances. In a $F = 1$ disc and taking $\rho_\bullet = 1\,\text{g cm}^{-3}$, we find $T_{\text{stop}} = 10^{-3}$ corresponds to particle sizes from $\sim 280\,\mu\text{m}$ at 10 au to $\sim 9\,\mu\text{m}$ at 100 au, or between ~ 3 mm and $90\,\mu\text{m}$ for $T_{\text{stop}} = 10^{-2}$.

4.2 Diagnostics

We analyse our simulation results using the diagnostics listed below. We denote mean value of a quantity Q by $\langle Q \rangle$. Unless otherwise stated, the spatial average is taken over the shell $|r - R_0| \le H_{g0}$. We also use $\text{rms}(Q)$ or $\sqrt{\langle Q^2 \rangle}$ to denote the root-mean-squared value of Q. Time-averaged values are denoted with an additional subscript t. Time is reported in units of the orbital period at R_0 and is denoted by P_0.

(i) The dust scaleheight H_d is obtained by fitting the dust density with

$$\rho_d(R, z) = \rho_d(R, 0) \exp \left(-\frac{z^2}{2H_d^2} \right), \quad (32)$$

where $\rho_d(R, 0)$ is the mid-plane dust density. We then normalize H_d by H_g.

(ii) The mid-plane dust-to-gas ratio $\epsilon_0 \equiv (\rho_d/\rho_g)_0$. We measure both average and maximum values within the sampling region.

(iii) The mid-plane vertical velocity v_{z0}.

(iv) Following Stoll et al. (2017), we measure the Reynolds stresses associated with vertical motions via

$$R_{z\phi} \equiv \rho v_z \Delta v_\phi, \quad (33)$$

where Δ denotes the deviation from the initial value. We then define the normalized vertical stress

$$\mathcal{R}_{z\phi} \equiv \frac{\text{rms}(R_{z\phi})}{c_{s0}^2 \langle \rho_i \rangle}, \quad (34)$$

as a dimensionless measure of the VSI strength, where ρ_i is the initial density field. Note that in time evolution plots below, the average is also taken over the height of the disc.

5 RESULTS

5.1 Lifting dust particles by the VSI

We first illustrate the effect of VSI turbulence on dust settling by varying the radial temperature gradient via the power-law index q. Here, we fix the particle size and metallicity such that $T_{\text{stop}} = 10^{-3}$ and $Z = 0.01$, respectively. Larger $|q|$ leads to stronger vertical shear and hence more vigorous VSI turbulence.
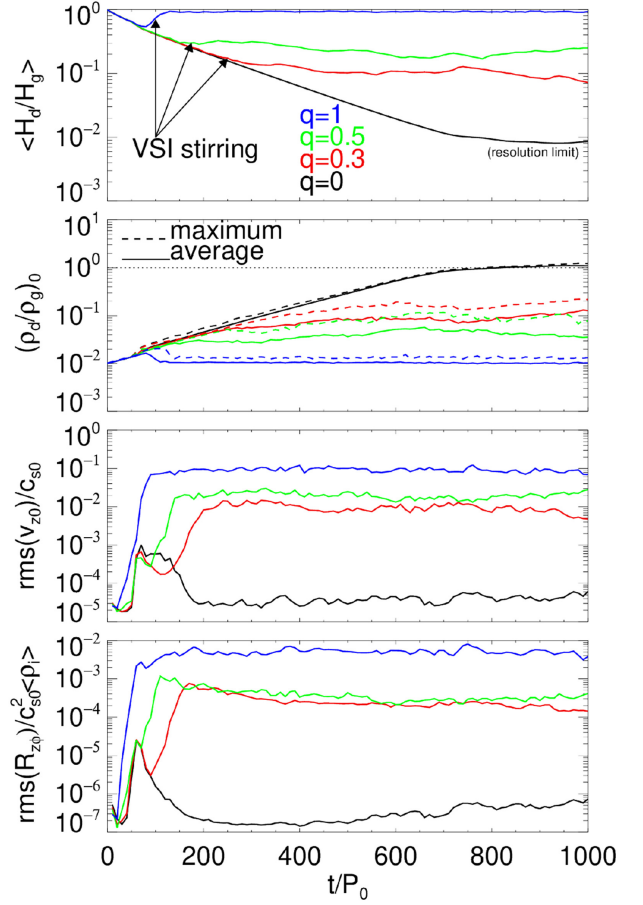

Figure 1. Top to bottom: evolution of dust-scaleheight, mid-plane dust-to-gas ratios, mid-plane vertical velocity, and vertical stress parameter; for different radial temperature gradients. The dotted horizontal line in the second panel indicates the critical dust-to-gas ratio, above which the streaming instability is expected to operate efficiently. The particle size and metallicity is fixed to $T_{\text{stop}} = 10^{-3}$ and $Z = 0.01$, respectively.

Fig. 1 shows the time evolution of the average dust scaleheight normalized by the gas scaleheight, $\langle H_d/H_g \rangle$; the average and maximum mid-plane dust-to-gas ratio, $\langle \epsilon_0 \rangle$ and $\max(\epsilon_0)$, respectively; the root-mean-squared mid-plane vertical velocity, $\sqrt{\langle v_{z0}^2 \rangle}$; and the dimensionless vertical stress, $\mathcal{R}_{z\phi}$; for $q = 0$, 0.3, 0.5, and 1. Fig. 2 compares several snapshots of the dust-to-gas ratio from these runs. It is evident that VSI turbulence hinders dust settling.

For $q = 0$ the disc is strictly isothermal and does not develop the VSI. In this laminar disc, dust settling proceeds until the resolution limit ($\simeq 10^{-2} H_g$) and $\epsilon_0 \sim 1$. Introducing moderate VSI turbulence with $q = 0.5$ prevents the dust from settling below $\sim 0.1 H_g$. Consequently ϵ_0 only increases to $O(0.1)$.

In the fully turbulent disc with $q = 1$ we find no signs of dust settling over the simulation time-scale. Fig. 2 shows in this case that dust remains well-mixed with the gas throughout the vertical disc column with $\rho_d/\rho_g \sim 10^{-2}$, with undulations near the surface. The banded structure in ρ_d/ρ_g with characteristic separation $\sim H_g/2$ is caused by the advection of dust particles by the large-scale up or down VSI motions, which have no vertical structure. This is shown in Fig. 3. The average vertical stress $\mathcal{R}_{z\phi} \simeq 5 \times 10^{-3}$ is consistent with Stoll et al. (2017), who found $\mathcal{R}_{z\phi} \lesssim 0.01$ for $|z| \le 2H_g$.
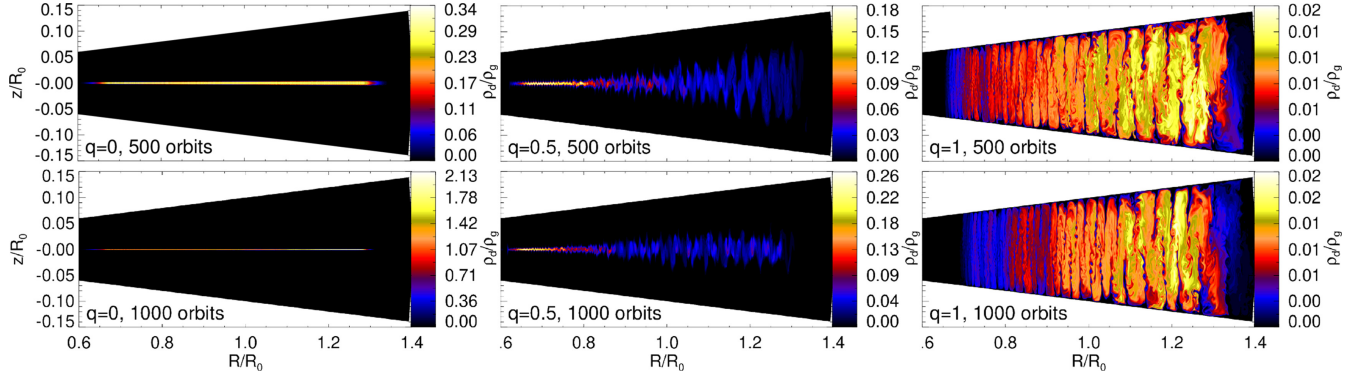
Figure 2. Effect of VSI turbulence on dust settling. The dust-to-gas ratio at $t = 500P_0$ (top) and $t = 1000P_0$ (bottom) are shown for discs with radial temperature profile indices $q = 0$ (left, no VSI), $q = 0.5$ (middle, moderate VSI), and $q = 1$ (right, strong VSI).
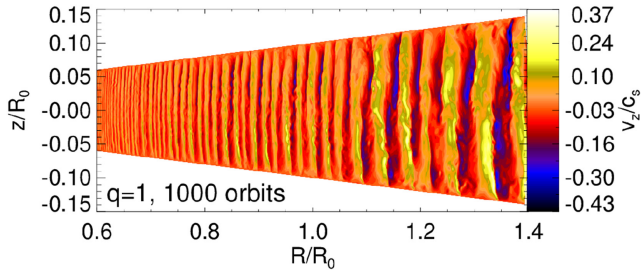

Figure 3. Vertical velocity at the end of the fiducial simulation with $(q, T_{stop}, Z) = (1, 10^{-3}, 10^{-2})$. The corresponding dust-to-gas ratio is shown in the bottom right-hand panel of Fig. 2.

In Fig. 4 we compare the time-averaged dust distribution and turbulence properties from a suite of runs with $q \in [0.1, 1]$. The averaging period is taken between when the system enters a quasi-steady state and the end of the simulation. We omit the $q = 0$ run here since in that case there is no physical steady state. We find $\langle H_d/H_g \rangle_t$ increases rapidly with q, but for $q \gtrsim 0.5$ the dust becomes well-mixed with $\langle H_d/H_g \rangle \simeq 1$ and $\langle \epsilon_0 \rangle_t \simeq 0.01$ ($=Z$ here). Notice the well-mixed and settled cases are separated by $\sqrt{\langle v_{z0}^2 \rangle}_t \sim \sqrt{T_{stop}} c_{s0}$ or $\mathcal{R}_{z\phi,t} \sim T_{stop}$. The former dependence is consistent with theoretical dust settling models, described below. As $\langle v_{z0}^2 \rangle_t$ and $\mathcal{R}_{z\phi,t}$ increases with $|q|$, this suggest that given a fixed particle size there exists a critical temperature gradient, $|q|_*$, below which dust-settling is allowed. However, as shown below, vertical stresses and velocities also depend on particle size and metallicity.

For comparison, we also plot in Fig. 4 the expected dust-scaleheight based on Dubrulle et al. (1995)'s model,

$$\frac{H_{d,model}}{H_g} = \left[1 + \frac{c_{s0}^2 \langle \Omega_K \tau_s \rangle_t}{\langle v_{z0}^2 \rangle_t \left(\Omega_K t_{eddy} \right)} \right]^{-1/2} \quad (35)$$

(see also Youdin & Lithwick 2007; Zhu et al. 2015), where the particle stopping time τ_s is measured at the disc mid-plane, and we regard the eddy time-scale t_{eddy} as a model parameter for simplicity. Setting $\Omega_K t_{eddy} = 0.15$ gives a good match to the measured $\langle H_d/H_g \rangle_t$ in the settled cases, while it somewhat underestimates the well-mixed cases. This value of t_{eddy} is similar to that found by Stoll and Kley (2016).
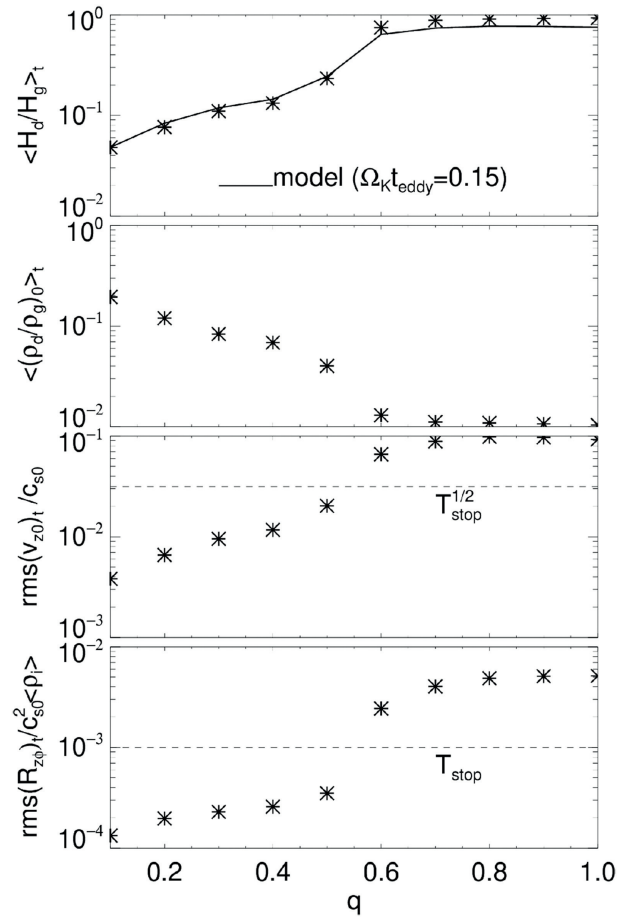

Figure 4. Top to bottom: time-averaged dust scaleheight, mid-plane dust-to-gas ratio, mid-plane vertical velocity, and vertical turbulence strength; as a function of the radial temperature gradient. The solid line in the top panel is obtained from equation (35). The particle size and metallicity is fixed to $T_{stop} = 10^{-3}$ and $Z = 0.01$, respectively.

5.2 Effect of particle size

We now examine the effect of particle size, which is parametrized by T_{stop} in our simulations. Here we fix $q = 1$ and $Z = 0.01$.

Fig. 5 compares the fiducial case with $T_{stop} = 10^{-3}$ to runs with 3, 5, and 10 times that particle size. Increasing T_{stop} allows faster
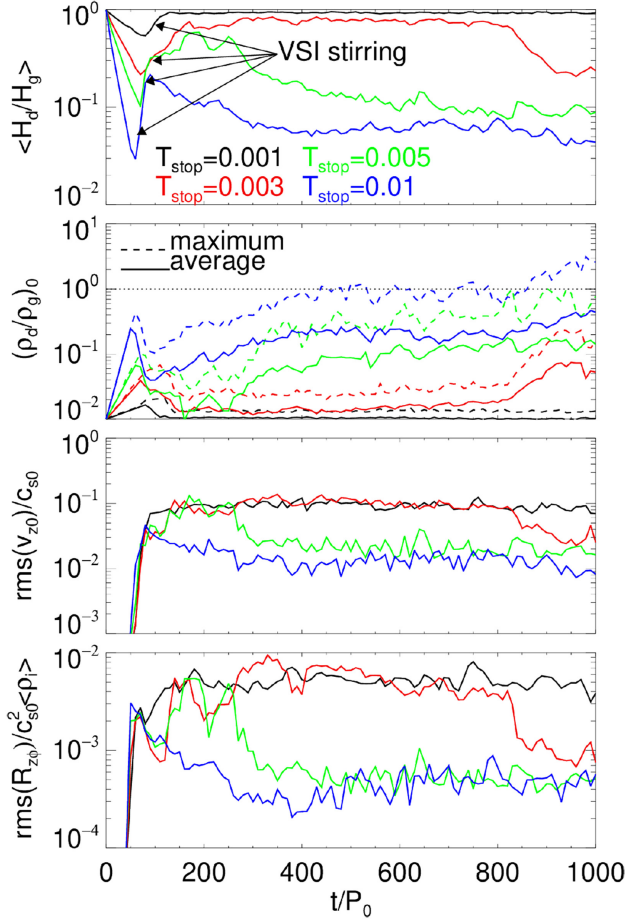
Figure 5. Top to bottom: evolution of dust-scaleheight, mid-plane dust-to-gas ratios, mid-plane vertical velocity, and vertical turbulence parameter; for different stopping times or particle size. The dotted horizontal line in the second panel indicates the critical dust-to-gas ratio, above which the streaming instability is expected to operate efficiently. The temperature profile and metallicity are fixed to $q = 1$ and $Z = 0.01$, respectively.

settling, since the settling speed $|v_{z,d}| \sim c_s T_{stop}$ (Takeuchi & Lin 2002). Larger particles can settle to a thinner layer before VSI-stirring, which begins at $t \sim 100P_0$ independently of T_{stop}. That is, the initial VSI growth rate is insensitive to particle size. However, VSI-stirring weakens with increasing T_{stop}, as $\langle H_d/H_g \rangle$ 'bounce' to smaller values with larger particles after the VSI activates. This is also reflected in the much smaller $\mathcal{R}_{z\phi}$ with $T_{stop} = 0.005$ and 0.01 compared to cases with $T_{stop} = 0.001$ and 0.003.

In the $T_{stop} = 0.003$ run, dust is almost perfectly remixed by the initial VSI. A quasi-steady state is apparently attained, but only until $t \sim 800P_0$, when we observe spontaneous settling. This is shown in Fig. 6, suggesting that the prior steady state was unstable. The $T_{stop} = 0.005$ and $T_{stop} = 0.01$ runs behave similarly. In both cases dust begins to settle soon after being remixed by the VSI. However, they also exhibit hints of spontaneous settling. The $T_{stop} = 0.005$ run attains a brief steady state ($150P_0 \lesssim t \lesssim 250P_0$) before settling, while at the end of the $T_{stop} = 0.01$ run $\langle \epsilon_0 \rangle$ suddenly increases. We discuss in Section 6.2 how spontaneous settling may be possible due to particle back-reaction.

Fig. 7 shows the final dust-to-gas ratio and vertical velocity distribution in the $T_{stop} = 0.01$ run. A dust clump develops at the outer boundary, possibly due to boundary conditions, which may
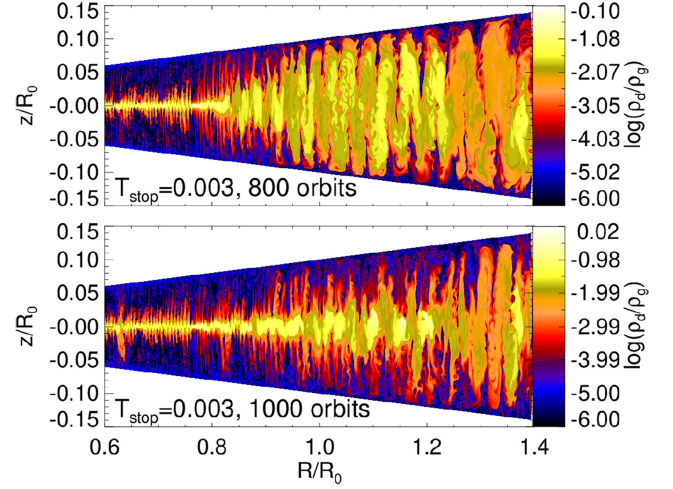
Figure 6. Spontaneous settling in the run with $T_{stop} = 0.003$. The disc remains in quasi-steady state with vertically well-mixed dust until $t \sim 800P_0$, after which the dust begins to settle.
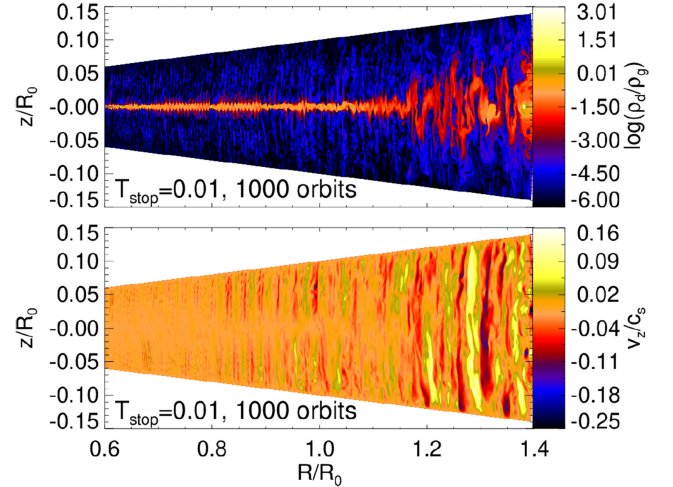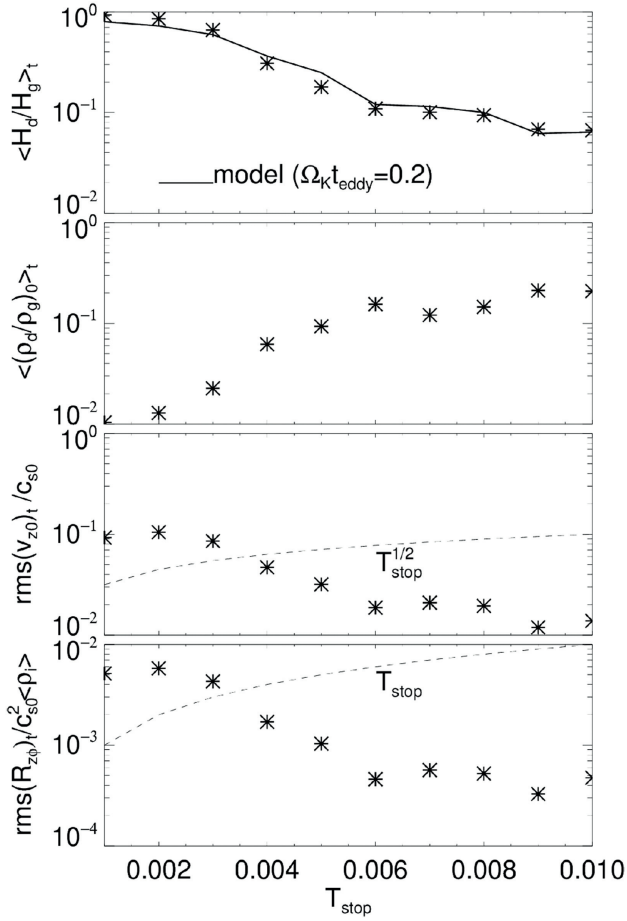

Figure 7. Dust-to-gas ratio (top) and vertical velocity (bottom) at the end of the simulation with $T_{stop} = 10^{-2}$.

be related to the increased dust mixing in $R \gtrsim 1.1R_0$. However, the sampling region around $R \simeq R_0$ is unaffected, and particles there have settled to a thin layer with little vertical motion, due to self-stabilization by dust-induced buoyancy (LY17).

Fig. 8 compares an extended set of simulations with varying T_{stop}. Here the time average is taken between the onset of the VSI and the end of the simulations. Significant settling occurs for $T_{stop} \gtrsim 0.005$, for which $\langle H_d/H_g \rangle_t$ drops to ~ 0.1 and $\langle \epsilon_0 \rangle_t \sim O(0.1)$. The measured $\langle H_d/H_g \rangle_t$ is consistent with the model described by equation (35) if we choose $\Omega_K t_{eddy} = 0.2$, again similar to eddy time-scales found by Stoll and Kley (2016). Although less clear-cut, this figure also indicates that dust settling occurs when $\sqrt{\langle v_{z0}^2 \rangle}_t \lesssim \sqrt{T_{stop}} c_{s0}$ or $\mathcal{R}_{z\phi,t} \lesssim T_{stop}$.

5.3 Effect of dust abundance

Dust-induced buoyancy is expected to help settling by stabilizing the VSI (LY17). Here we investigate this effect more precisely by varying the solid abundance or metallicity $Z = \Sigma_d/\Sigma_g$. Larger Z
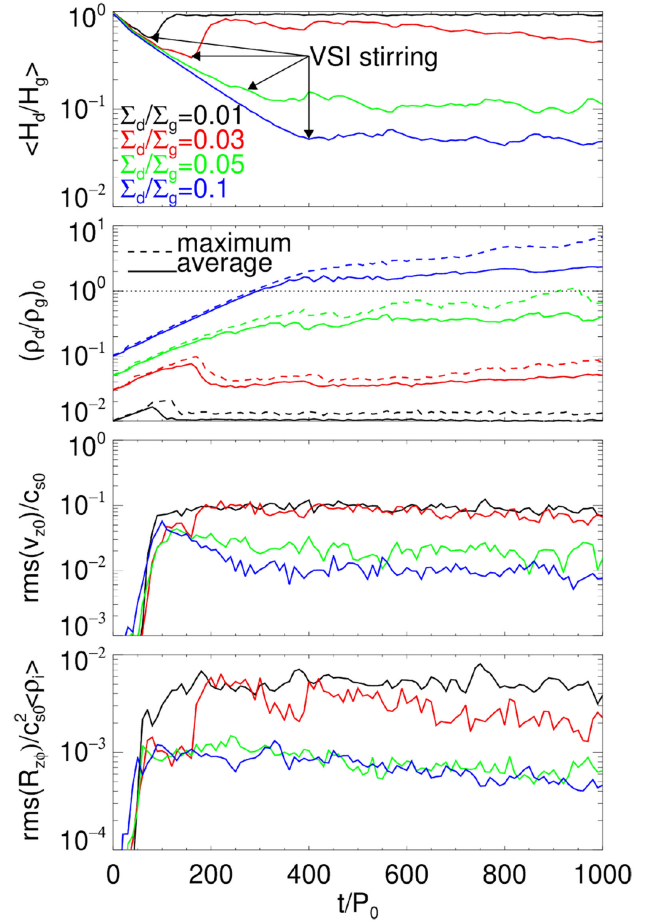
Figure 8. Top to bottom: time-averaged dust scaleheight, mid-plane dust-to-gas ratio, mid-plane vertical velocity, and vertical turbulence strength; as a function of the particle size parametrized by T_{stop}. The solid line in the top panel is obtained from equation (35). The radial temperature gradient and metallicity is fixed to $q = 1$, $Z = 0.01$, respectively.


Figure 9. Top to bottom: evolution of dust-scaleheight, mid-plane dust-to-gas ratios, mid-plane vertical velocity, and vertical turbulence parameter; for different metallicities. The dotted horizontal line in the second panel indicates the critical dust-to-gas ratio, above which the streaming instability is expected to operate efficiently. The radial temperature gradient and particle size is fixed to $q = 1$ and $T_{stop} = 10^{-3}$, respectively.

corresponds to stronger dust feedback on to the gas. For our fiducial parameter values $(q, T_{stop}, Z) = (1, 10^{-3}, 10^{-2})$ dust does not settle. We thus consider $Z \in [0.01, 0.1]$ in this section. In Appendix A we demonstrate the VSI is particularly sensitive to dust-loading in weakly turbulent discs, in which case the stabilizing effect of feedback manifests even with ϵ_0 of a few per cent.

Fig. 9 compares the disc evolution for $Z = 0.01, 0.03, 0.05$, and 0.1. Increasing Z does not affect the settling time-scale. Instead, larger Z delays the VSI, which allows the dust to settle to a thinner layer. This reflects the stabilizing effect of particle back-reaction. For $Z = 0.03$, the VSI remixes the dust at $t \sim 200P_0$, and settles slowly afterwards. For $Z = 0.05$ and $Z = 0.1$, the initial VSI only halts the settling process, and does not increase $\langle H_d/H_g \rangle$, unlike the $Z = 0.01$ and $Z = 0.03$ runs.

For $Z = 0.1$, we find $\langle \epsilon_0 \rangle \sim 2$ for $t \gtrsim 300P_0$. This is expected to develop the SI, but our numerical set-up and resolution is insufficient to resolve the SI for the small particles considered here (Yang & Johansen 2016). In the $Z = 0.05$ and $Z = 0.03$ runs, $\langle \epsilon_0 \rangle$ does not reach unity within the simulation time-scale, but is still significantly enhanced relative to the $Z = 0.01$ run. Comparing these runs to the previous simulations with increased T_{stop} (Fig. 5) show that increasing Z is more effective in raising the dust-to-gas ratio than increasing particle size. This is not surprising since, for a given H_d

a larger Z implies a larger ϵ_0 (equation 20), let alone in the present cases where a smaller dust scaleheight is reached with increasing Z compared to the same increase in T_{stop}.

The $Z = 0.05$ and $Z = 0.1$ cases show much reduced mid-plane vertical velocities and vertical turbulence compared to $Z = 0.01$, which is consistent with the former cases reaching much smaller values of $\langle H_d/H_g \rangle$. The $Z = 0.1$ run also displays a slow drop in $\mathcal{R}_{z\phi}$ for $t \gtrsim 400P_0$, with a corresponding rise in $\langle \epsilon_0 \rangle$, while $\langle H_d/H_g \rangle$ remains relatively constant. This signifies particle settling into mid-plane unhindered, in fact this settling is stabilizing the system. The $Z = 0.03$ run attains $\mathcal{R}_{z\phi} \simeq 5 \times 10^{-3}$ early on, similar to the $Z = 0.01$ case, but it eventually drops to $\mathcal{R}_{z\phi} \simeq 2 \times 10^{-3}$. This also reflects the slow settling observed after the initial VSI in that case.

Fig. 10 shows ρ_d/ρ_g and v_z at the end of the $Z = 0.1$ simulation. Maximum vertical velocities are reduced by at a factor of two from the standard case with $Z = 0.01$ (Fig. 3), while mid-plane values are reduced by an order of magnitude (Fig. 9). Similar to the large-particle simulation (Fig. 7), the dust mid-plane is quiescent, although not completely inactive. This dense dust layer also decouples the upper, dust-free region from that in the lower disc.
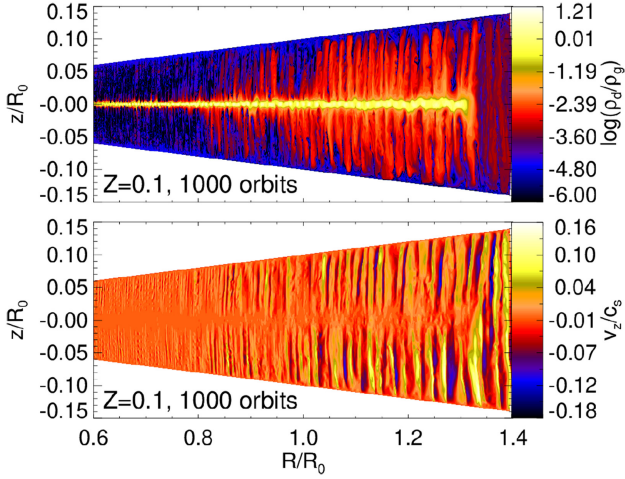
Figure 10. Dust-to-gas ratio (top) and vertical velocity (bottom) at the end of the simulation with $Z = 0.1$.
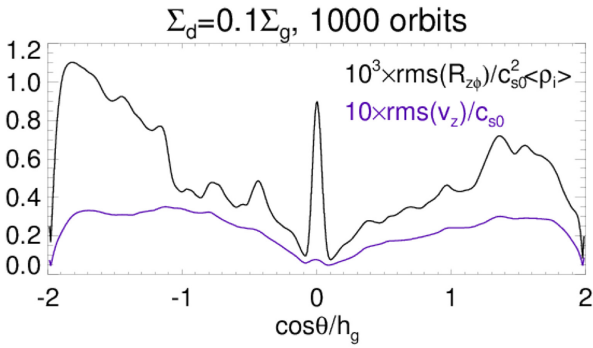

Figure 11. Vertical stress (black) and vertical velocity (purple) profiles at the end of the $Z = 0.1$ simulation.

Fig. 11 shows the corresponding vertical stress and vertical velocity profiles. Vertical stresses generally increase away from the mid-plane, reaching $\mathcal{R}_{z\phi} \sim 10^{-3}$ near the boundaries. This reflects VSI activity in the dust-poor layers above and below the mid-plane. The spike at $z = 0$ is associated with the fact that the dust layer rotates closer to the Keplerian speed compared to the initially gas-dominated state. (Recall from equation 33 that $R_{z\phi} \propto \Delta v_\phi$.) Although vertical velocities are reduced towards the mid-plane, notice that $v_{z0} \neq 0$. Such residual mid-plane vertical motions are due to disturbance by bulk vertical motions from the VSI-active layers (the mid-plane dust layer in itself is expected to be stable; see below). This explains why the dust layer maintains a finite thickness and does not settle further.

5.3.1 Dust-induced buoyancy

Fig. 12 compares the vertical buoyancy frequency and vertical shear profiles at the end of the $Z = 0.1$ simulation. We show both the actual vertical shear rate, $\left|R\partial_z\Omega^2\right|$, and that associated with the imposed temperature gradient, $\left|R\partial_z\Omega^2\right|_{\mathrm{temp}}$, as estimated from equation (28). This quantity is the driver of the underlying VSI (LY17) and is essentially constant in time. On the other hand, the total vertical shear displayed in Fig. 12 is either dominated by the settled dust in the mid-plane or by VSI modes away from it.
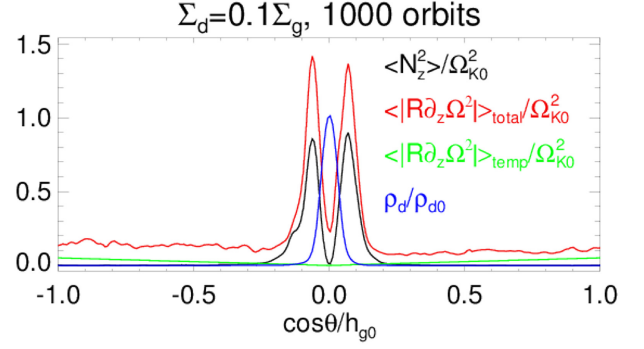
Figure 12. Vertical profiles in the squared vertical buoyancy frequency (black; equation 17), vertical shear rate (total: red; temperature-related: green; equation 28), and dust density (blue; normalized to the mid-plane value) at the end of the $Z = 0.1$ simulation.
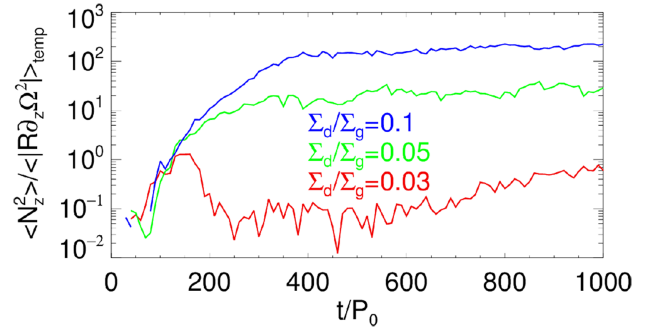
Figure 13. Comparison between the stabilizing effect of dust-induced buoyancy (equation 17) to the destabilizing effect of the temperature-related vertical shear (equation 28), as a function of the metallicity. The averages are taken over the dust layer.

The total vertical shear exceeds buoyancy throughout the disc column. However, recall in axisymmetric discs that dust-induced vertical shear *does not* cause instabilities (LY17). Thus in our simulations instability is associated with vertical shear induced by the imposed temperature gradient, $\left|R\partial_z\Omega^2\right|_{\mathrm{temp}}$. Away from the mid-plane at $|z| \gtrsim 0.1\,H_g$, buoyancy frequencies vanish, whereas the temperature-related, destabilizing vertical shear rate is larger there. About the mid-plane ($|z| \sim 0.1\,H_g$), however, this destabilizing effect is overwhelmed by the stabilizing buoyancy. This explains the 'layered' structure seen in Fig. 10: a quiet mid-plane with VSI-active layers above and below it.

Fig. 13 compares the stabilizing buoyancy to the destabilizing temperature-related vertical shear, averaged over the dust layer for several cases. We omit the $Z = 0.01$ run here since $N_z^2 \sim 0$ in that case. For $Z = 0.03$ this ratio is $\lesssim 1$, though rising later on, which is consistent with the slow settling. For $Z = 0.05$ and $Z = 0.1$ this ratio is $\gg 1$, and the VSI is strongly stabilized by buoyancy within the dust layer.

5.3.2 Dust settling by dust-loading

We now examine the critical metallicity for dust settling to overcome the VSI. Fig. 14 compares quasi-steady states as a function of Z. We also plot several cases with $q = 0.5$.

For $q = 1$ we find stabilization by dust-loading is most dramatic for $Z \simeq 0.03$–0.05, while for $Z > 0.05$ dust settles to $\langle H_d/H_g \rangle_t \lesssim 0.1$
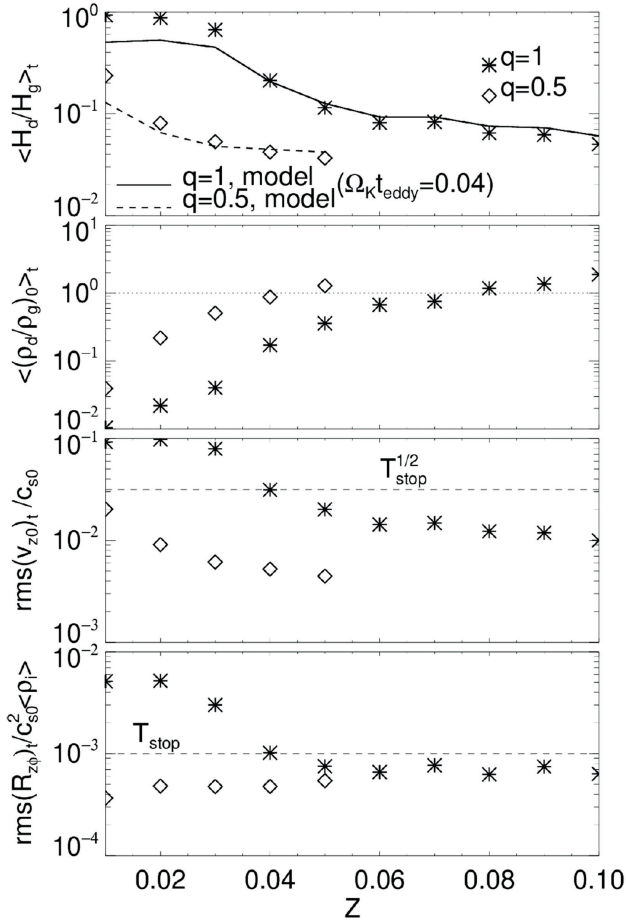
Figure 14. Top to bottom: time-averaged dust-scaleheight, mid-plane dust-to-gas ratio, mid-plane vertical velocity, and vertical turbulence strength as a function of the metallicity. The radial temperature gradient is $q = 1$ (asterisks) and $q = 0.5$ (diamonds). The solid (dashed) line in the top panel is obtained from equation (35) for the $q = 1$ ($q = 0.5$) cases. The dotted horizontal line in the second panel indicates the critical dust-to-gas ratio, above which the streaming instability is expected to operate efficiently. The particle size is fixed to $T_{stop} = 10^{-3}$.

with little variation with respect to Z. On the other hand, for $q = 0.5$ dust can settle to $\langle H_d/H_g \rangle_t \lesssim 0.1$ with $Z \gtrsim 0.02$, suggesting the critical Z for settling scales as $\sim 1/|q|$. We find the settled dust scaleheights can be fitted with equation (35), but this required $\Omega_K t_{eddy} \simeq 0.04$, which is smaller than that found by Stoll and Kley (2016). This indicates that increasing the metallicity reduces the turbulence eddy time-scales. We find $\sqrt{\langle v_{z0}^2 \rangle_t} \sim \sqrt{T_{stop}} c_{s0}$ continues to distinguish between settled and well-mixed cases as we vary the metallicity.

In the settled cases, we find the dust layer is too thin to affect the average vertical stress $\mathcal{R}_{z\phi,t}$, i.e. the measured vertical turbulence is associated with the gas layers above and below the mid-plane, hence $\mathcal{R}_{z\phi,t}$ flattens off. Nevertheless, we find settled cases still obey $\mathcal{R}_{z\phi,t} \lesssim T_{stop}$.

These results indicate that in weakly VSI-turbulent discs, dust settling is sensitive to the local metallicity. This implies that small changes in Z, for example due to radial drift and pile-up of dust, could have significant impact on dust settling in disc regions with shallow temperature profiles (see Section 6 for a discussion).

6 DISCUSSION

6.1 Overcoming VSI turbulence through particle back-reaction

Our simulations indicate that particle back-reaction on to the gas is important for dust settling in discs prone to the VSI. This implies that previous studies using passive particles may have overestimated the minimum particle sizes that can settle in VSI-active discs (Stoll & Kley 2016; Flock et al. 2017).

We find that raising the metallicity $Z = \Sigma_d/\Sigma_g$, which increases the particle back-reaction, helps dust settling. In this case the settling speed is unaffected. Instead, VSI stirring is increasingly delayed due to stabilization by dust-induced buoyancy forces. This results in thinner dust layers before the VSI halts the settling process, which are even more difficult to stir up. (The same effect occurs for increasing particle size.)

For $T_{stop} = 10^{-3}$ and $q = 1$ we find $Z \gtrsim 0.05$ is needed for dust to settle down to $H_d \lesssim 0.1 H_g$, while in less turbulent discs with $q = 0.5$ this only required $Z \gtrsim 0.02$, slightly above the solar value. This suggests that in weakly turbulent discs the VSI is sensitive to the disc metallicity. This is consistent with the argument presented in Section 3.2 and the simulation in Appendix A, which shows that the VSI can be stabilized when the dust-to-gas ratio ϵ becomes comparable to the disc's aspect-ratio h_g, i.e. a few per cent in PPDs.

Our simulations show that H_d generally depends on q, T_{stop}, and Z. All three parameters affect the VSI turbulence strength $\mathcal{R}_{z\phi}$ (the dimensionless vertical Reynolds stress) and the mid-plane vertical velocity v_{z0}. We find that the settled and well-mixed cases are separated by $\mathcal{R}_{z\phi} \sim T_{stop}$ or $\sqrt{\langle v_{z0}^2 \rangle} \sim \sqrt{T_{stop}} c_s$. The latter condition is consistent with the settling model of Dubrulle et al. (1995), provided an appropriate eddy time-scale is chosen (see equation 35).
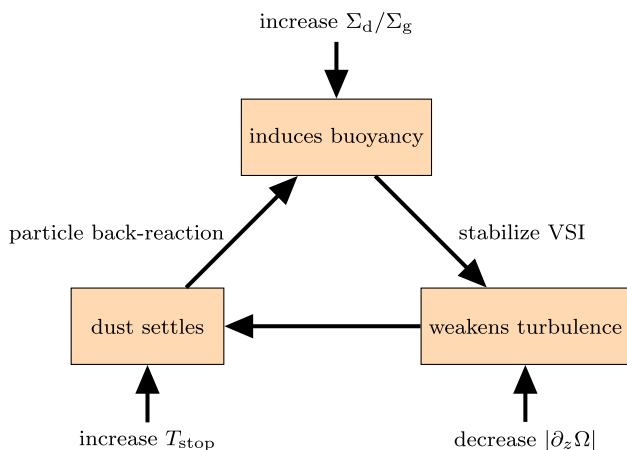
We can apply the above results to assess whether particles of a given T_{stop} (>0) and abundance Z can settle. Recent analyses indicate $|v_z| \sim h_g|q|c_s$ for VSI turbulence (Barker & Latter 2015; Latter & Papaloizou 2018), which is consistent with our simulations. We thus expect particles with $T_{stop} \gtrsim h_g^2 q^2$ to settle, even in the limit $Z \to 0$. However, if $T_{stop} \lesssim h_g^2 q^2$, then $Z \gtrsim h_g|q|$ is needed to weaken the VSI and enable dust settling (see Section 3.2).

6.2 Self-sustained settling

We propose particle back-reaction can lead to self-sustained dust settling, as illustrated in Fig. 15. In this picture, dust settles if it can induce an effective buoyancy that stabilizes the VSI, which favours further settling, and the cycle repeats. This feedback cycle may be initiated by increasing T_{stop} via particle growth, raising the local metallicity Z via radial dust drift, or reducing the radial temperature gradient $|q|$. The last trigger is less likely in PPDs at large radii because the local temperature profile is fixed by stellar irradiation.

We suggest this positive feedback loop is responsible for spontaneous settling observed in some simulations (e.g. Fig. 6). The quasi-steady balance between VSI-stirring and dust settling is delicate because the VSI is sensitive to buoyancy. If the system is perturbed such that Z increases locally, then that region may begin to settle and enter the feedback loop.

However, self-sustained settling does not continue indefinitely. As dust settles to the mid-plane, it leaves behind dust-free, VSI-turbulent layers above and below it. Vertical motion from the active layers continue to disturb or distort the mid-plane dust layer, eventually halting further sedimentation.

increase Σ_d/Σ_g

induces buoyancy

particle back-reaction

stabilize VSI

dust settles

weakens turbulence

increase T_{stop}

decrease $|\partial_z \Omega|$

Figure 15. Self-sustained settling of dust in VSI-active discs. A positive feedback loop is enabled by particle back-reaction on to the gas. This allows dust settling to induce buoyancy forces to stabilize the VSI, which reduces the turbulent stirring, leading to further settling.

Indeed, we find that although $|v_z|$ drops significantly with decreasing $|z|$, it is still non-zero about the dusty mid-plane. Such a layered structure in $|v_z|$ is characteristic of settled dust in VSI-prone discs. In fact, a similarly layered structure is found in the linear VSI with a dusty mid-plane (LY17; see their Section 6.3). This picture is analogous to layered accretion discussed by Gammie (1996), although in that case it is the radial mass accretion rate that is minimized in the magnetic dead zones near the mid-plane. Dust settling in the dead zone is halted by residual activity induced by the turbulent active layers (Fromang & Papaloizou 2006). We suggest a similar effect is present in our simulations: the VSI active layers induce residual vertical motions at the disc mid-plane to maintain a finite dust layer thickness.

In reality, self-sustained settling may also be terminated by other processes, such as the KHI (Chiang 2008; Lee et al. 2010), GI (Goldreich & Ward 1973), or SI (Youdin & Goodman 2005). However, these effects are not captured by our numerical models.

6.3 Implications for planetesimal formation

Efficient planetesimal formation via rapid SIs require a mid-plane dust-to-gas ratio of order unity or larger (Youdin & Goodman 2005; Johansen et al. 2009b).

However, our results indicate small particles would remain lofted by VSI turbulence. Here, what constitutes as 'small' depends on the turbulence strength and local metallicity. In the outer parts of PPDs, VSI turbulence is primarily related to the local temperature gradient $|q|$. If we take $|q| \simeq 1$ and solar metallicity $Z = 0.01$, then by small we mean particles with T_{stop} of $O(10^{-3})$. At a distance of 20 au, this roughly corresponds to particle sizes of $O(10^2 \, \mu m)$, assuming an internal density $\rho_\bullet = 1 \, g \, cm^{-3}$ (see equation 31).

In the above example, particles smaller than $\sim 100 \, \mu m$ will remain lofted. However, if they can grow to $\sim$mm sizes amidst the turbulence, e.g. by sticking (Blum 2018), or if the local metallicity increases (e.g. due to a radial pile-up of dust, Kanagawa et al. 2017), then these particles can settle against the VSI and eventually undergo SI.

Raising the local metallicity is an effective way to achieve a local dust-to-gas ratio $\rho_d/\rho_g \sim 1$ in two regards. First, a larger Z allows $\epsilon_0 \sim 1$ to be attained at larger H_d (see equation 20). That is, the required degree of settling is smaller. Secondly, increasing

Z actively stabilizes the disc against the VSI, thereby allowing for effective settling.

Coincidentally, non-linear numerical simulations of the SI indicate $Z \gtrsim 0.02$ is required for strong clumping of particles with $T_{stop} \sim 0.01$–0.1 (Johansen et al. 2009b; Bai & Stone 2010a), while smaller particles with $T_{stop} \sim 10^{-3}$ require $Z \gtrsim 0.04$ (Yang et al. 2017). These particle clumps can then undergo GI. One also requires $Z \gtrsim 0.03$ in order to overcome the KHI associated with dust-induced vertical shear, which would overturn the dust layer (Chiang 2008; Lee et al. 2010).

We conclude that in the outer parts of protoplanetary discs, small particles must have supersolar metallicities in order to form planetesimals self-consistently: dust can then settle against VSI turbulence, trigger efficient streaming instability, clump, and finally undergo gravitational collapse.

6.4 Application to observations

Our simulations may aid the interpretation of PPD observations. As a concrete example, we consider the PPD around HL Tau (ALMA Partnership et al. 2015). This inclined disc displays well-defined dust rings at all azimuth, which implies that the dust has settled.

For the HL Tau disc, Pinte et al. (2016) estimates $H_d \sim 0.07 H_g$ at 100 au, and $\epsilon_0 \sim 0.2$ assuming $Z = 0.01$. They infer a dimensionless vertical diffusion parameter $\alpha \simeq 3 \times 10^{-4}$, assuming passive particles (Fromang & Nelson 2009). Interestingly, these values are consistent with our $T_{stop} = 0.01$ simulation[2] shown in Fig. 8, if we identify α as our dimensionless vertical Reynolds stress. Using equation (31), $T_{stop} = 0.01$ corresponds to particle sizes $\sim 90 \, \mu m$ at 100 au, similar to that adopted in the HL Tau disc model of Jin et al. (2016). For mm-sized particles, $T_{stop} = 0.01$ requires a disc ~ 10 times more massive than the MMSN, or grains with internal density $\sim 0.1 \, g \, cm^{-3}$.

For dusty VSI turbulence we find $H_d = H_d(q, T_{stop}, Z)$. This may be used to estimate the local metallicity. For example, let us assume $q \simeq 0.5$ and particle sizes of $\sim 100 \, \mu m$, and a massive (young) disc with $F = 10$. This gives $T_{stop} \simeq 10^{-3}$ at 100 au. Then Fig. 14 suggests Pinte et al. (2016)'s estimate, $H_d \simeq 0.07 H_g$, can be achieved with $Z \simeq 0.03$. On the other hand, if $Z \sim 10^{-3}$ so that particle back-reaction is negligible, then VSI turbulence would be too strong to allow dust to settle (see e.g. Flock et al. 2017).

The interplay between VSI turbulence, dust settling, and the local metallicity may lead to a radially-dependent dust-scaleheight, as follows. Suppose dust drifts radially, say from R_2 to R_1 such that $Z(R_1) > Z(R_2)$. Then the increased (decreased) metallicity at R_1 (R_2) would stabilize (destabilize) the disc there. Now, if the gas density contrast between R_1 and R_2 is smaller than that in Z, i.e. $Z_1/Z_2 > \Sigma_{g1}/\Sigma_{g2}$, so that the contrast in stopping times is outweighed by that in metallicity, then dust settling (mixing) should be promoted at R_1 (R_2). Ultimately, $H_d(R_1) < H_d(R_2)$, assuming similar gas scaleheights if $R_1 > R_2$. That is, dust rings should have smaller scaleheights compared to dust gaps[3]. This can be tested with future observations of the radial and vertical dust structure in PPDs.

---

[2]Note that we used $(q, h_g) = (1, 0.05)$ while Pinte et al. (2016) and Jin et al. (2016) assumed $(q, h_g) = (0.7, 0.1)$ and $(0.43, 0.096)$, respectively. However, the destabilizing effect of increasing $|q|$ offsets the stabilizing effect of decreasing h_g (Nelson et al. 2013).

[3]However, if the gas density in the dust ring is also increased significantly, then the decreased stopping times may negate the positive effect of increased metallicity on settling.

6.5 Caveats and outlooks

Below we discuss several caveats of our modelling and directions for future work.

We assumed axisymmetry throughout. This simplification over-estimates the strength of VSI turbulence (Manger & Klahr 2018). For example, Stoll and Kley (2016) found that passive particles with $T_{stop} = 0.002$ can settle to $H_d \simeq 0.66\,H_g$, whereas we find such particles remain perfectly mixed with the gas. On the other hand, Stoll and Kley found particles with $T_{stop} = 0.02$ only settles to $H_d \simeq 0.4H_g$, whereas we find $T_{stop} = 0.01$ particles can already settle to $H_d \lesssim 0.1H_g$, which could be due to the stabilizing effect of particle back-reaction in our case.

Axisymmetric models also suppress vortex formation due to the VSI (Richard, Nelson & Umurhan 2016; Manger & Klahr 2018), as well as the KHI due to the vertical shear between the dust and gas layers (Chiang 2008). Vortices are known to act as effective dust traps (Lyra & Lin 2013), although they can also source hydrodynamic turbulence (Lesur & Papaloizou 2009, 2010). The KHI may become relevant if the dust layer becomes sufficiently thin and/or if the overall metallicity is large (see Appendix B). It will be necessary to perform full 3D simulations to investigate how these additional processes affect dust settling.

We adopted initial disc models that minimized radial disc evolution in order to focus on vertical dust settling (Section 2; see also CL18). However, in PPDs dust typically drifts inward. This may be important for dust settling because radial pile-up of dust, should it occur, would stabilize the VSI and induce dust settling. Future work should explore different initial dust and gas density profiles.

The dust-gas model of LY17 only allows for a single species of dust particles. In reality, there will be a distribution of particle sizes, each with a different metallicity. Particles that are larger or more abundant will settle first, which is expected to stabilize the system. The settling of smaller particles may then ensue. To investigate this scenario, one would need a dust-gas framework that allows for multiples species of dust grains.

7 SUMMARY

In this paper we study the sedimentation of small dust particles in the outer parts of protoplanetary discs subject to hydrodynamic turbulence driven by the vertical shear instability (VSI). We perform 2D, axisymmetric numerical simulations to investigate the effect of VSI turbulence strength, $\mathcal{R}_{z\phi}$ (essentially the vertical Reynolds stress-to-pressure ratio), particle size or Stokes number, T_{stop}, and solid abundance (metallicity) Σ_d/Σ_g on dust settling.

We model VSI turbulence explicitly by imposing a fixed radial temperature gradient q. However, we find the resulting stress $\mathcal{R}_{z\phi}$ can also depend on T_{stop} and Σ_d/Σ_g. Nevertheless, our results indicate that dust settles when the resulting $\mathcal{R}_{z\phi} \lesssim T_{stop}$. In our simulations this is equivalent to having a mid-plane vertical velocity dispersion $\sqrt{\langle v_{z0}^2 \rangle} \lesssim \sqrt{T_{stop}}c_s$. The latter condition is consistent with the classic dust settling model of Dubrulle et al. (1995).

We find that dust settling is favoured by (1) weaker VSI turbulence, corresponding to shallower radial temperature profiles, (2) larger particles, and (3) increased local metallicity. We expect dust can settle if $T_{stop} \gtrsim h_g^2 q^2$ or $\Sigma_d \gtrsim h_g |q| \Sigma_g$, where h_g is the disc aspect-ratio.

Our simulations show that particle back-reaction plays an important role for dust settling against the VSI. This is because dust-loading, specifically vertical gradients in the dust-to-gas ratio, introduces a buoyancy force (LY17), which is known to be effective in stabilizing the VSI (LY15). Thus settled dust is strongly self-stabilized against the VSI. This results in a quiescent dusty mid-plane with residual vertical velocities induced by VSI turbulence from the gaseous layers above and below it, which maintains the dust layer thickness.

We find dust settling can overcome the VSI by increasing the local metallicity. For particles with $T_{stop} = 10^{-3}$, corresponding to grain sizes of $\sim 100\,\mu m$ at 20 au in MMSN-like discs, we find that $\Sigma_d \gtrsim 0.04\Sigma_g$ enables dust reach $\rho_d \sim \rho_g$ at the disc mid-plane. Such metallicities are also expected to trigger planetesimal formation via the streaming instability (Johansen et al. 2009b; Yang et al. 2017). Our results are thus consistent with the notion that planetesimals can form from small dust particles in the outer parts of protoplanetary discs, provided that the corresponding solid abundance is a few times larger than the solar value.

REFERENCES

Alexander R., Pascucci I., Andrews S., Armitage P., Cieza L., 2014, in Beuther H., Klessen R. S., Dullemond C. P., Henning T., eds, Protostars and Planets VI. Univ. Arizona Press, Tuscon, p. 475
ALMA Partnership et al., 2015, ApJ, 808, 10
Bai X.-N., 2016, ApJ, 821, 80
Bai X.-N., Stone J. M., 2010a, ApJ, 722, 1437
Bai X.-N., Stone J. M., 2010b, ApJ, 722, L220
Balbus S. A., Hawley J. F., 1991, ApJ, 376, 214
Balsara D. S., Tilley D. A., Rettig T., Brittain S. D., 2009, MNRAS, 397, 24
Barge P., Sommeria J., 1995, A&A, 295, L1
Barker A. J., Latter H. N., 2015, MNRAS, 450, 21
Barranco J. A., 2009, ApJ, 691, 907
Blum J., 2018, Space Sci. Rev., 214, 52
Chen J.-W., Lin M.-K., 2018, MNRAS, 478, 2737 (CL18)
Chiang E., 2008, ApJ, 675, 1549
Chiang E., Youdin A. N., 2010, Annu Rev. Earth Planet. Sci., 38, 493
Dittrich K., Klahr H., Johansen A., 2013, ApJ, 763, 117
Dubrulle B., Morfill G., Sterzik M., 1995, Icarus, 114, 237
Flock M., Nelson R. P., Turner N. J., Bertrang G. H.-M., Carrasco-González C., Henning T., Lyra W., Teague R., 2017, ApJ, 850, 131
Fromang S., Lesur G., 2017, preprint (arXiv:1705.03319)
Fromang S., Nelson R. P., 2009, A&A, 496, 597
Fromang S., Papaloizou J., 2006, A&A, 452, 751
Gammie C. F., 1996, ApJ, 457, 355
Gammie C. F., 2001, ApJ, 553, 174
Gibbons P. G., Rice W. K. M., Mamatsashvili G. R., 2012, MNRAS, 426, 1444
Goldreich P., Ward W. R., 1973, ApJ, 183, 1051
Gonzalez J.-F., Laibe G., Maddison S. T., 2017, MNRAS, 467, 1984
Helled R. et al., 2014, in Beuther H., Klessen R. S., Dullemond C. P., Henning T., eds, Protostars and Planets VI, Univ. Arizona Press, Tuscon, p. 643

Jacquet E., Balbus S., Latter H., 2011, MNRAS, 415, 3591
Jin S., Li S., Isella A., Li H., Ji J., 2016, ApJ, 818, 76
Johansen A., Youdin A., 2007, ApJ, 662, 627
Johansen A., Henning T., Klahr H., 2006, ApJ, 643, 1219
Johansen A., Youdin A., Klahr H., 2009a, ApJ, 697, 1269
Johansen A., Youdin A., Mac Low M.-M., 2009b, ApJ, 704, L75
Johansen A., Blum J., Tanaka H., Ormel C., Bizzarro M., Rickman H., 2014, in Beuther H., Klessen R. S., Dullemond C. P., Henning T., eds, Protostars and Planets VI. Univ. Arizona Press, Tuscon, p. 547
Kanagawa K. D., Ueda T., Muto T., Okuzumi S., 2017, ApJ, 844, 142
Klahr H., Hubbard A., 2014, ApJ, 788, 21
Klahr H., Pfeil T., Schreiber A., 2018, in Deeg H., Belmonte J., eds, Handbook of Exoplanets. Springer International Publishing AG, p. 138
Laibe G., Price D. J., 2014a, MNRAS, 440, 2136
Laibe G., Price D. J., 2014b, MNRAS, 444, 1940
Latter H. N., 2016, MNRAS, 455, 2608
Latter H. N., Papaloizou J., 2018, MNRAS, 474, 3110
Lee A. T., Chiang E., Asay-Davis X., Barranco J., 2010, ApJ, 718, 1367
Lesur G. R. J., Latter H., 2016, MNRAS, 462, 4549
Lesur G., Papaloizou J. C. B., 2009, A&A, 498, 1
Lesur G., Papaloizou J. C. B., 2010, A&A, 513, A60
Lin M.-K., Youdin A. N., 2015, ApJ, 811, 17 (LY15)
Lin M.-K., Youdin A. N., 2017, ApJ, 849, 129 (LY17)
Lissauer J. J., 1993, ARA&A, 31, 129
Lyra W., 2014, ApJ, 789, 77
Lyra W., Lin M.-K., 2013, ApJ, 775, 17
Lyra W., Umurhan O., 2018, PASP, preprint (arXiv:1808.08681)
Manger N., Klahr H., 2018, MNRAS, 480, 2125
Marcus P. S., Pei S., Jiang C.-H., Barranco J. A., Hassanzadeh P., Lecoanet D., 2015, ApJ, 808, 87
Mignone A., Bodo G., Massaglia S., Matsakos T., Tesileanu O., Zanni C., Ferrari A., 2007, ApJS, 170, 228
Mignone A., Flock M., Stute M., Kolb S. M., Muscianisi G., 2012, A&A, 545, 16
Nakagawa Y., Sekiya M., Hayashi C., 1986, Icarus, 67, 375
Nelson R. P., Gressel O., Umurhan O. M., 2013, MNRAS, 435, 2610
Pinilla P., Youdin A., 2017, in Pessah M., Gressel O., eds, Astrophysics and Space Science Library, Vol. 445, Formation, Evolution, and Dynamics of Young Solar Systems. Springer, Berlin, p. 91
Pinte C., Dent W. R. F., Ménard F., Hales A., Hill T., Cortes P., de Gregorio-Monsalvo I., 2016, ApJ, 816, 25
Price D. J., Laibe G., 2015, MNRAS, 451, 813
Raettig N., Klahr H., Lyra W., 2015, ApJ, 804, 35
Raymond S. N., Kokubo E., Morbidelli A., Morishima R., Walsh K. J., 2014, in Beuther H., Klessen R. S., Dullemond C. P., Henning T., eds, Protostars and Planets VI. Univ. Arizona Press, Tuscon, p. 595
Rice W. K. M., Lodato G., Pringle J. E., Armitage P. J., Bonnell I. A., 2004, MNRAS, 355, 543
Richard S., Nelson R. P., Umurhan O. M., 2016, MNRAS, 456, 3571
Riols A., Lesur G., 2018, A&A, 617, 22
Safronov V. S., 1969, Evoliutsiia doplanetnogo oblaka. Nauka, Moscow
Shi J.-M., Chiang E., 2013, ApJ, 764, 20
Shi J.-M., Zhu Z., Stone J. M., Chiang E., 2016, MNRAS, 459, 982
Simon J. B., Armitage P. J., Li R., Youdin A. N., 2016, ApJ, 822, 55
Squire J., Hopkins P. F., 2018, MNRAS, 477, 5011
Stoll M. H. R., Kley W., 2014, A&A, 572, 12
Stoll M. H. R., Kley W., 2016, A&A, 594, 17
Stoll M. H. R., Kley W., Picogna G., 2017, A&A, 599, 4
Takahashi S. Z., Inutsuka S.-i., 2014, ApJ, 794, 7
Takeuchi T., Lin D. N. C., 2002, ApJ, 581, 1344
Umurhan O. M., Shariff K., Cuzzi J. N., 2016, ApJ, 830, 95
Weidenschilling S. J., 1977, MNRAS, 180, 57
Whipple F. L., 1972, in Elvius A., ed., Plasma to Planet. Wiley, New York, p. 211
Yang C.-C., Johansen A., 2016, ApJS, 224, 39
Yang C.-C., Johansen A., Carrera D., 2017, A&A, 606, A80
Yang C.-C., Mac Low M.-M., Johansen A., 2018, ApJ, 868, 27
Youdin A. N., Goodman J., 2005, ApJ, 620, 459

Youdin A., Johansen A., 2007, ApJ, 662, 613
Youdin A. N., Lithwick Y., 2007, Icarus, 192, 588
Zhu Z., Stone J. M., Bai X.-N., 2015, ApJ, 801, 81

APPENDIX A: DUST SETTLING WITH NEGLIGIBLE BACK-REACTION

It is common to model dust in PPDs as passive particles when the dust-to-gas ratio $\epsilon \ll 1$ (e.g. Stoll & Kley 2016; Flock et al. 2017). Here we demonstrate that this condition is problem-dependent, and it alone may be insufficient to justify neglecting particle back-reaction. Specifically, we show that feedback has significant impact in weakly VSI-turbulent discs.

We consider a disc with $q = 0.3$ and particles with $T_{stop} = 10^{-3}$. Fig. A1 compares the simulation with $Z = 10^{-2}$, as presented in the main text, to a disc with $Z = 10^{-3}$. They evolve similarly until $t \sim 200\,P_0$, at which point dust in the $Z = 10^{-3}$ disc undergoes complete remixing by the VSI, whereas dust continues to settle in the $Z = 10^{-2}$ disc. In the latter case $\langle \epsilon_0 \rangle \simeq 0.04 \ll 1$ at $t = 200\,P_0$, but this is apparently sufficient to overcome the VSI. As explained in Section 3.2, this is because the VSI is sensitive to buoyancy forces induced by vertical gradients in the dust-to-gas ratio. Even an ϵ of order $h_g \ll 1$ can provide effective stabilization against the VSI.
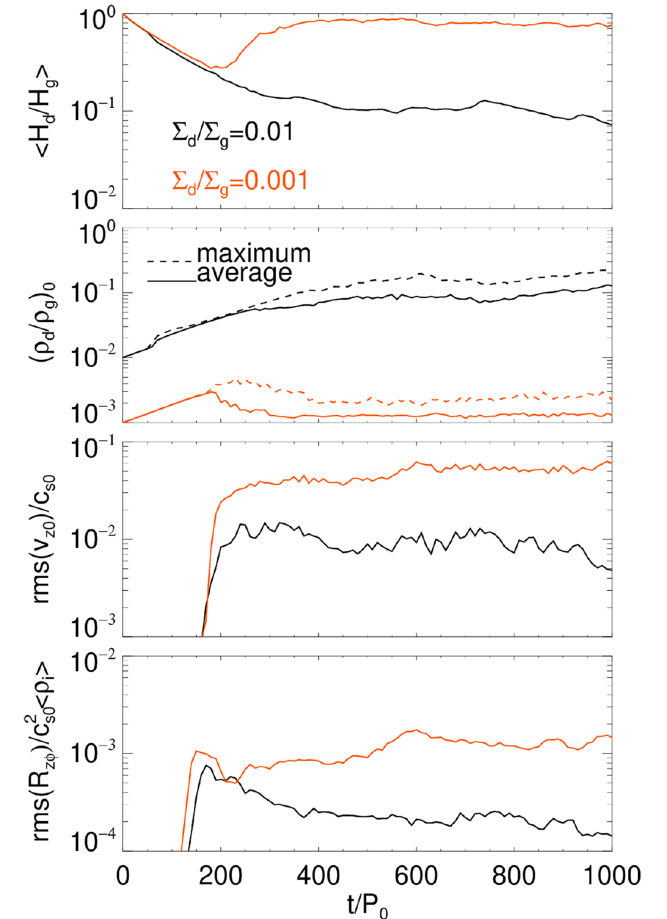

Figure A1. Top to bottom: evolution of dust-scaleheight, mid-plane dust-to-gas ratios, mid-plane vertical velocity, and vertical turbulence parameter; in discs with metallicity $Z = 10^{-3}$ (orange) and $Z = 10^{-2}$ (black, as considered in the main text). The radial temperature profile and particle size is fixed to $q = 0.3$ and $T_{stop} = 10^{-3}$, respectively.

APPENDIX B: KELVIN–HELMHOLTZ INSTABILITIES

Axisymmetric simulations preclude Kelvin–Helmholtz instabilities associated with the vertical shear between a dusty mid-plane and the dust-free gas above and below it (Chiang & Youdin 2010; Lee et al. 2010). Nevertheless, we can use the axisymmetric profiles reached in our simulations to examine stability against the KHI. In the literature this is usually assessed through the Richardson number, $Ri = N_z^2/(\partial_z v_\phi)^2$. Numerical simulations find KHI occurs for $Ri \lesssim Ri_*$, where the critical value Ri_* depends on the dust layer parameters (Lee et al. 2010).

Fig. B1 shows the evolution of Ri in selected simulations where dust settles down to a few per cent of H_g. For $Z = 0.01$ Lee et al. (2010) finds $Ri_* \sim 0.1$, which is smaller than that the corresponding simulations. These cases are therefore stable against the KHI. However, extrapolating the numerical results of Lee et al. (2010) gives $Ri_* \simeq 2$ for $Z = 0.1$, whereas we find $Ri = 1$–2 in this case. The $Z = 0.1$ simulation may thus be marginally unstable to KHI. Full 3D simulations will be required to check this.
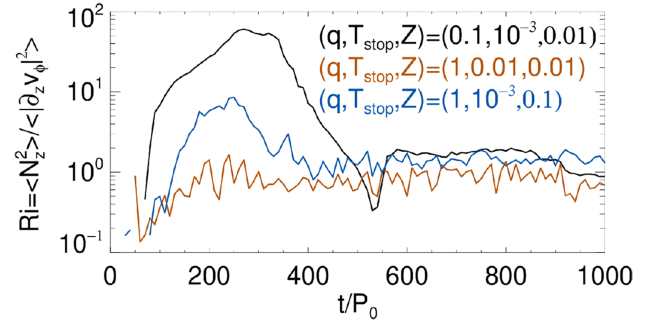
Figure B1. Evolution of the Richardson number in the dust layer, for simulations where significant dust settling occurs.

This paper has been typeset from a TEX/LATEX file prepared by the author.